THE JOURNAL OF PHYSICAL CHEMISTRY Letters

pubs.acs.org/JPCL Letter

Surface Oxidation Modulates the Interfacial and Lateral Thermal Migration of MXene ($Ti_3C_2T_x$) Flakes

Qi Zhang,[¶] Yu Chen,[¶] Yifan Zhang,[¶] Jingyong Sun, Mingjun Hu, Xin Yan,* Kaijun Yuan,* Xueming Yang, and Jiebo Li*

Cite This: *J. Phys. Chem. Lett.* 2020, 11, 9521−9527 Read Online

ACCESS | Metrics & More | Article Recommendations | Supporting Information

ABSTRACT: The thermal management of MXene ($Ti_3C_2T_x$) plays a crucial role in its performance during various emerging applications. However, it is unclear how the inevitable oxidation structure of $Ti_3C_2T_x$ influences the thermal dissipation, which might hinder its long-term performance and even create thermal damage. Here we show the thermal migration of a $Ti_3C_2T_x$ flake with surface oxidation in film and water by combining ultrafast pump−probe technique with molecular dynamics (MD) simulations. The results demonstrate that the oxidation at the surface could facilitate interfacial thermal migration with shorter interfacial distances but would block the lateral thermal transfer. Besides, our results also identified that the slight oxidation could not obviously change the thermal decay of $Ti_3C_2T_x$ nanosheets in water due to similar hydrogen bonds between water and interface. The research not only provides fundamental understanding of the thermal dissipation of MXene but also benefits for designing the thermal dissipation system to the MXene device.

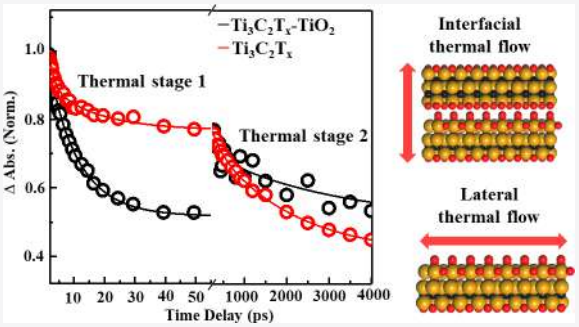

As a novel type of transition metal-based 2D material, the most popular MXene ($Ti_3C_2T_x$) has been endowed amazing prospects in versatile fields,[1] including energy storage,[2] electromagnetic interference shielding,[3] electronics,[4] and photon-detectors.[5] In these emerging applications, the electron moving at electrodes would accompany the generation of internal heat and localized temperature rise inside these $Ti_3C_2T_x$ flakes, bringing the systematic risks and limitations for the performances.[6,7] To avoid or alleviate the thermal damage at $Ti_3C_2T_x$ flakes, it is required to deeply understand the microscopic mechanism that how the thermal energy of the hot flakes transfer to other flakes. Moreover, the scientific significance of this heat conduction research is also applicable to photothermal therapy,[8−10] photoactuator,[11] and solar energy conversion.[12] In these applications, the photon energy is absorbed by the flake and transferred to the surrounding environment after high efficiency photothermal conversion. Overall, understanding the thermal energy dissipation of the most widely used $Ti_3C_2T_x$ nanosheet is very important for the development of MXene related applications.

In general, the surface terminated groups and interfacial interactions with surrounding molecules were crucial to the out-of-plane energy migration at MXene interface.[13] Noticeably, $Ti_3C_2T_x$ oxidation at the surface is inevitable.[14] Even at room temperature with the moisture and air, part of $Ti_3C_2T_x$ is gradually oxidized to TiO_2 nanoparticles at flake surface, forming the $Ti_3C_2T_x$−TiO_2 composite.[15−17] Once oxidation starts, the defects and wrinkles could provide nucleation sites for continuing oxidation.[18] Besides, heat and light illumination would significantly facilitate the oxidation.[19] Thus, during many long-term $Ti_3C_2T_x$ applications, the effective material would be the $Ti_3C_2T_x$−TiO_2 composite. Even if the $Ti_3C_2T_x$−TiO_2 composite could be applied in the photocatalysis,[20] solid electrolyte interphase,[21] and environment sensing,[22] it also might hamper the utilities of $Ti_3C_2T_x$ in other numerous applications. Furthermore, this oxidation thus might be a potential major challenge of overheating MXene-based devices. This topic has been majorly overlooked. Thus, it is critical to capture thermal transport for partially oxidized $Ti_3C_2T_x$ flakes.

In this work, we employed molecular dynamic (MD) simulations and ultrafast pump probe technique to investigate how the surface oxidation alter the interfacial and lateral thermal migration of $Ti_3C_2T_x$ flakes. Our results showed that the interface thermal migration would be facilitated with oxidized TiO_2 on the $Ti_3C_2T_x$ surface in the film. The faster interfacial thermal conductions of $Ti_3C_2T_x$ with oxidized TiO_2 was due to the shorter interlayer distance of two flakes. In contrast, the lateral heat flow could be decelerated by the oxidation. In addition, the results also confirmed in solution 5% surface modification with TiO_2 could not retard or

Received: September 21, 2020
Accepted: October 15, 2020
Published: October 28, 2020

https://dx.doi.org/10.1021/acs.jpclett.0c02886
J. Phys. Chem. Lett. 2020, 11, 9521−9527

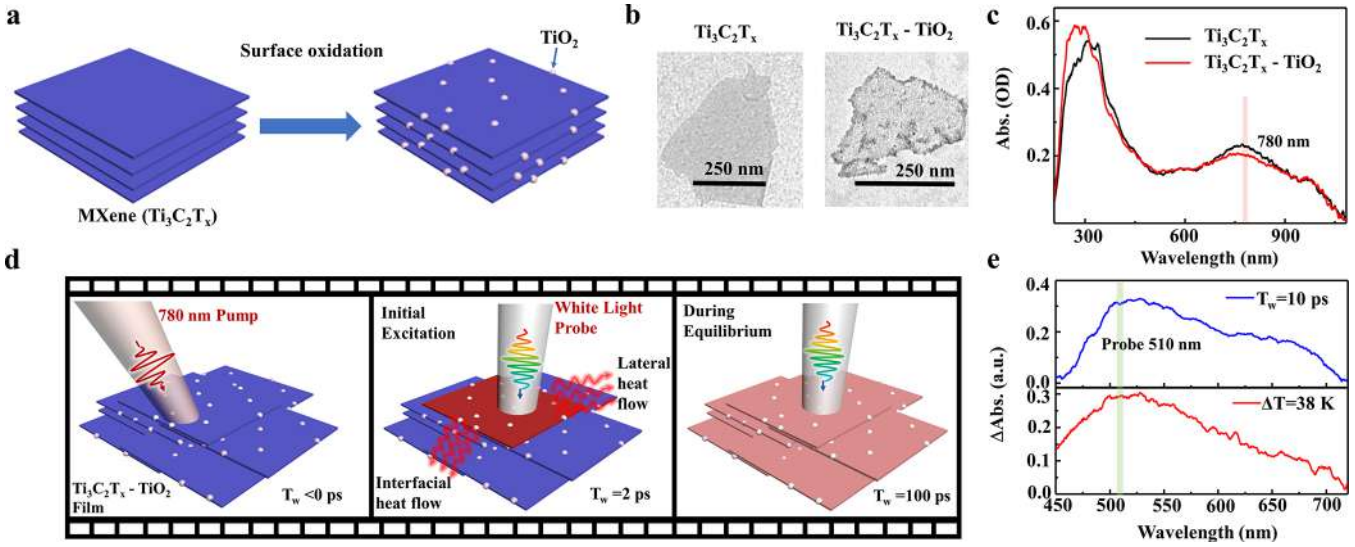

Figure 1. (a) Scheme of surface oxidation on $Ti_3C_2T_x$. (b) TEM of $Ti_3C_2T_x$ and partially oxidized $Ti_3C_2T_x$. (c) Spectrum of the two samples in water. (d) Scheme of ultrafast spectroscopy to measure the thermal dissipation of these samples. (e) Comparison of transient spectrum of $Ti_3C_2T_x$ at 10 ps (upper) and temperature different spectrum difference (A = absorption spectral intensity at 333 K minus the absorption spectral intensity at 295 K) of $Ti_3C_2T_x$ sample (below).

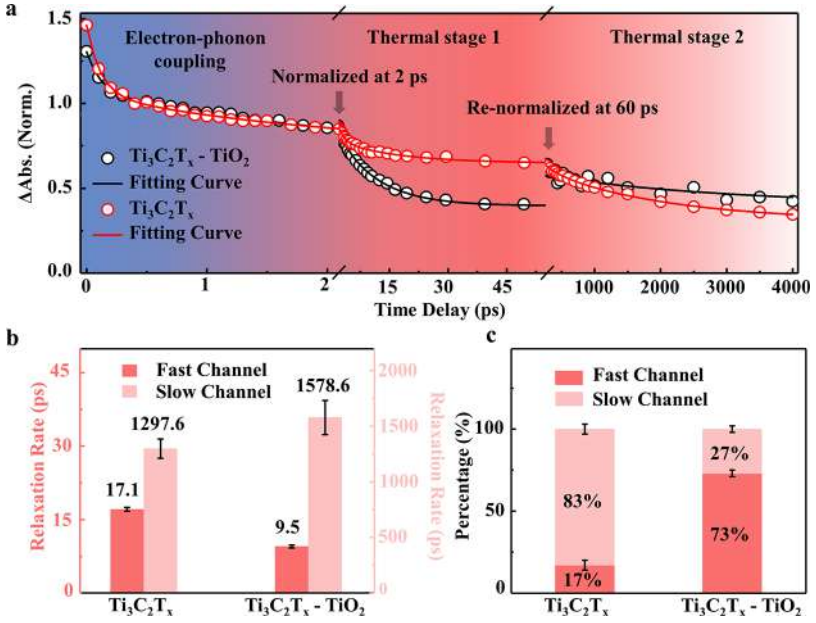

Figure 2. (a) Dynamic curves and fitting thermal dissipations. Dots are experimental data and lines are fitting curves. (b) Relaxation time constants for the two samples under two thermal relaxation channels. (c) Ratios of the two channels during the total relaxations.

accelerate the energy migration from $Ti_3C_2T_x$ to water. MD simulation confirmed that the hydrogen bonding dominated the migration process in solution. The results allow us to determine a relationship between surface oxidation and thermal dissipation control, which could be potentially used to understand the $Ti_3C_2T_x$ related thermal applications.

The preparing sample details and ultrafast spectroscopy experimental method have been described in supporting note 1. To obtain the partially oxidized $Ti_3C_2T_x$, we applied the laser illumination method[18] on the $Ti_3C_2T_x$/water solution to facilitate the oxidation at the surface, shown in Figure 1a. The TEM in Figure 1b showed that the oxidation of $Ti_3C_2T_x$ could produce some nanoparticles on the surface. With the HETEM shown in Figure S1, the nanoparticles are assigned as TiO_2 with rutile structure. In this sample, TiO_2 could cover ~5% of the flake surface, shown in Figure S1. Thus, we named the partial oxidation sample as "$Ti_3C_2T_x$–TiO_2" in Figure 1b and the following studies. The partial oxidation at the surface could decrease the absorption of $Ti_3C_2T_x$ at 780 nm and increase the absorption at 260 nm, shown in Figure 1c. Thus, we had two comparable samples: $Ti_3C_2T_x$ and $Ti_3C_2T_x$–TiO_2. To capture the thermal dissipation dynamics of $Ti_3C_2T_x$ in the two samples, we then employed the ultrafast spectroscopy shown in Figure 1d. The pump pulse was set to 780 nm ($Ti_3C_2T_x$ absorption peak), generating $Ti_3C_2T_x$ to the excited electronic state. The following board band probe pulse could track the transient spectrum intensity of the nonequilibrium shown in Figure 1d. As shown in Figure S2, the broadband negative

https://dx.doi.org/10.1021/acs.jpclett.0c02886
J. Phys. Chem. Lett. 2020, 11, 9521−9527

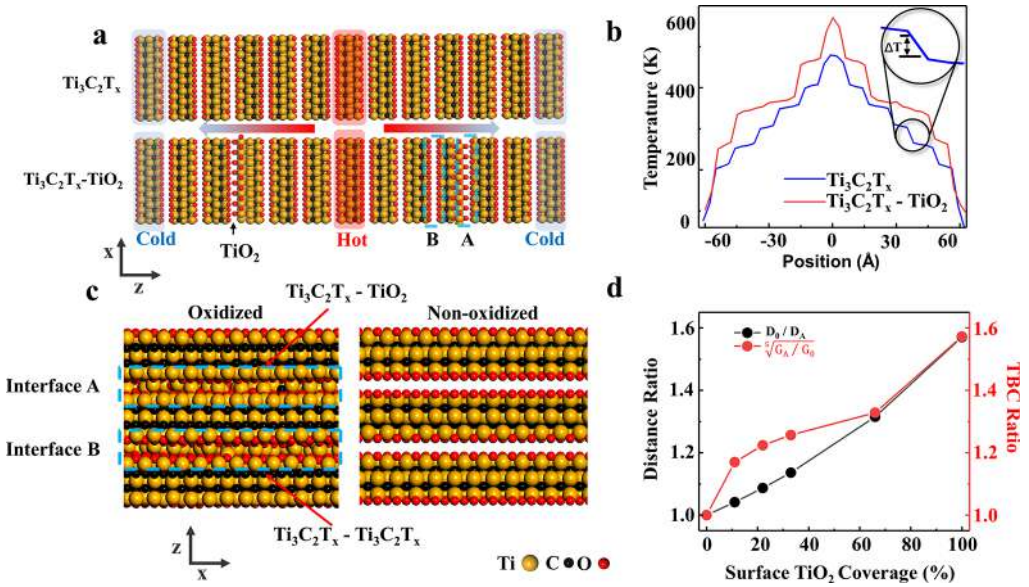

Figure 3. (a) Atomistic structure of the $Ti_3C_2T_x$ stacking model. The dashed blue box A and B represent the initial structure of Interface A and B (shown in (c)). (b) Calculated temperature profile, the ΔT is exploited for calculating the thermal boundary conductance (TBC). (c) Zoomed-in atomistic visualization of oxidized structure and nonoxidized structure after structure relaxation. Interface A is the interface of original $Ti_3C_2T_x$ and partial oxidized $Ti_3C_2T_x$ ($Ti_3C_2T_x$–TiO_2, the initial structure is shown in dashed box A in (a)) and interface B interface of $Ti_3C_2T_x$ and $Ti_3C_2T_x$ (the initial structure is shown in dashed box B in (a)). (d) Variation of TBC ratio and boundary distance ratio with respect to TiO_2 coverage.

signal with the peak centered at ∼780 nm could be attributed to the photobleaching due to the photoexcitation and the positive absorption band ranging from 450 to 700 nm centered at ∼510 nm, which was attributed to the photoinduced absorption signal. Figure 1e (upper) showed that the 510 nm peak after 2 ps represented thermal induced absorption of the flake because that is almost identical with the temperature different spectrum shown in Figure 1e (below). The temperature different spectra originate from increasing temperature to result in a change of the dielectric constant. Thus, its dynamics would be applied to analyze two directions of thermal energy dissipation at hot flakes. In addition, the signal intensity was proportional to the pump laser intensity, shown in Figure S3. In this experimental work, we mainly investigated these two samples in solid films (around 100 nm thickness in Figure S4) and water solutions. The entire dynamic process after photon energy injection was shown in Figure 2. After excitation, the produced hot electronic state was generated before 100 fs. The hot electrons could damp to Femi level electrons within ∼200 fs.[23] Then the excited electronic energy could convert into inside phonons ($Ti_3C_2T_x$ lattice motion) within ∼2 ps.[23−25] During this electron−phonon coupling process, we found that oxidation did not alter the electron dynamic pathway, as shown in Figure 2a. After 2 ps, all the photon energy absorbed by $Ti_3C_2T_x$ had been converted into the lattice motions inside flakes. In other words, the pump pulse created "hot" $Ti_3C_2T_x$ nanosheets. Because the heat could flow either vertically across the flakes or laterally transfer in plane, we numerically divided the hot surface relaxation pathways into two channels. Thus, we applied the biexponential decay function to fit the thermal decay pathways as $C(t) = C_0 + C_1 \exp(-t/t_1) + C_2 \exp(-t/t_2)$. We then could define two thermal stages (fast channel and slow channel) during the hot flake thermal relaxation because the parameters in the fast channel are 2 orders faster than the second channels for both samples. At the first thermal stage, we surprisingly found that the oxidation of the $Ti_3C_2T_x$ surface would significantly facilitate $Ti_3C_2T_x$ thermal dissipation. If no oxidation occurred at the surface, the dynamic decay time constant of the fast channel was around 17.1 ± 0.4 ps. The oxidation altered the thermal dissipation time constant to 9.5 ± 0.3 ps, which was much faster than the nonoxidization sample. After the signal intensities were renormalized at 60 ps as maximum values, the dynamic trends of the two samples would switch after 60 ps, as shown in thermal stage 2 in Figure 2a. The oxidation sample could be fitted with a decay rate around 1578 ps^{-1}, and the clean flakes sample could be fitted with a decay rate around 1297 ps^{-1}. Due to the existence of the fast channel, more than 70% thermal energy could dissipate through thermal stage 1 at oxidation sample. On the contrary, most thermal energy (∼83%) of the clean flake then dissipated at thermal stage 2. Overall, the oxidation at the surface made distinctive different thermal dissipation pathways on $Ti_3C_2T_x$ nanosheets in two directions.

To understand the molecular level of these thermal stages, we applied molecular dynamics simulation to investigate two directions, thermal dissipations of $Ti_3C_2T_x$ flakes with different extents of oxidation. The detail of the MD atomistic simulation model has been described in supporting note 2. We first constructed the interfacial heat conduction model with stacking layers of $Ti_3C_2O_2$, as shown in Figure 3a. The blue dashed box A indicated the interface of original $Ti_3C_2T_x$ and partially oxidized $Ti_3C_2T_x$. The dashed box B indicated the interface beside the partially oxidized surface. In this simulation, we adopted reverse nonequilibrium molecular dynamics (RNEMD, further discussion about RNEMD can be found in supporting note 3 and Figure S5). Until the temperature profile achieved equilibrium, the interfacial heat conductance was evaluated with thermal boundary conductance (TBC, detailed introduction of TBC can be found in the Supporting Information). Each jump (ΔT) of the temperature profile in Figure 3b (blue curve) represented heat transfers across interface. The TBC values of all the interfaces were almost the same, and the calculated value was 243 MW/(m^2

https://dx.doi.org/10.1021/acs.jpclett.0c02886
J. Phys. Chem. Lett. 2020, 11, 9521−9527

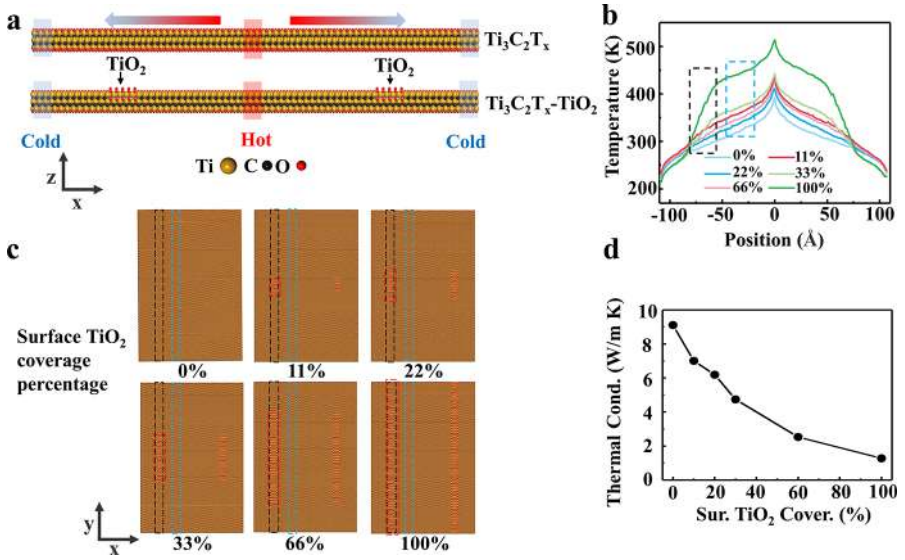

Figure 4. (a) Atomistic structure of lateral thermal conduction model. (b) Calculated temperature profile of different TiO_2 coverage. The blue dashed box represents nonoxidized area, and the black dashed box represents partial oxidized area. (c) Atomistic visualization of partial oxidized structures. The red dashed box represents the oxidized part, and the rest of the area in the black dashed box is nonoxidized. (d) Variation of thermal conductivity with respect to TiO_2 coverage.

K) on average. For the oxidized $Ti_3C_2T_x$ (one side of a layer of $Ti_3C_2T_x$ in the interface was oxidized, red line in Figure 3b), the temperature jump decreased substantially between the oxidized surface and nonoxidized surface. On the basis of these data, we found the TBC for the interface with the oxidized surface on one side (interface A in Figure 3c) was 1.5 times slower than the TBC for the interface without the oxidized surface (interface B in Figure 3c). Please notice that interfaces A and B in Figure 3c are snapshots from the equilibrated structure, and they correspond to the blue dashed boxes A and B in Figure 3a (initial structure). We then analyzed the detailed structure change at the interface with the partially oxidized surface. After structure relaxation, the space between two layers was reduced (Figure 3c). A similar observation could be found in stacked graphene and hexagonal boron nitride heterostructures.[26] Further bonding analysis showed that there were newly generated Ti−O bonds between interfaces A and B; the number of Ti−O bonds increased by 42% after oxidation (Figure 3c). In other words, the existence of TiO_2 became a bridge that combined two layers of $Ti_3C_2T_x$. The structures and temperature profiles of different oxidation ratios were shown in Figures S6 and S7, respectively, and the average boundary distances of interfaces A and B with different oxidation ratios were listed in Table S1. In our previous study, we studied the relation of the energy transfer rate constant (k_{DA}, defined in Supporting note 3) and the distance between the energy donor and acceptor (r_{DA}).[27] Here, we use this model to quantitatively analyze our simulation result. We computed the distance change ratio (D_0/D_A, D_0 was the nonoxidized boundary distance, and D_A was the oxidized boundary distance) and the root of TBC change ratio ($\sqrt[n]{G_A/G_0}$, n = 3, 4, 5, or 6). G_A was the TBC of the oxidized flake, and G_0 was the TBC of the nonoxidized flake. In Figure 3d, we found D_0/D_A matched the value of the $\sqrt[5]{G_A/G_0}$, which denoted the oxidized interface interaction was more consistent with mechanical coupling (from the previous investigation, in the mechanical coupling mechanism, the transfer rate constant is inversely proportional to r_{DA}^n; n can be 3, 4, 5, or 6). A more detailed plot of the distance change ratio and the root of the TBC change ratio can be found in Figure S8.

Meanwhile, the amount of the newly generated Ti−O bonds between the interface increased along with more oxidations (the results can be found in Figures S9 and S10). Overall, the oxidation at the interface strengthened the interfacial interaction between two layers with reduced distance and increased bonds. Therefore, the MD results confirmed that the surface oxidation facilitated the interfacial thermal conductance between flakes, consistent with the ultrafast experimental thermal relaxation stage 1. It is worthwhile to mention a recent report that discussed how machine learning can be combined with computation and experiments to understand the correlations between structures and properties of 2D materials.[28] After the fast-interfacial thermal migration between flakes, the remaining thermal energy would dissipate via lateral heat transport. Macroscopically, $Ti_3C_2T_x$ and TiO_2 have different thermal conductivities.[29,30] In order to evaluate the effect of oxidation on the lateral heat transport, we adopt thermal conductivity to evaluate the thermal energy transportation within the surface. As shown in Figure 4a, RNEMD simulations were performed in the x direction.

After the system reached the steady state, we obtained the temperature profile of different $Ti_3C_2O_2$ monolayers in the x-direction (Figure 4b). As shown in Figure 4c, we varied the TiO_2 percentage from 0 to 100% in the y direction in a belt on the surface of MXene. The results showed that for the nonoxidized part of different flakes, there was no distinct change ($dT/dx \approx 1.0$ K/Å) of the slope (blue dashed box) on the temperature curve. However, with the top surface of the flake partially oxidized, the slope (black dashed box) of the temperature profile changed from 1.0 to 5.6 K/Å. Then the average thermal conductivity of the flakes could be calculated. Noticeably, as shown in Figure 4d, accompanied by oxidation varying from 0% to 100%, the thermal conductivity value would decrease 7 times, dropping from 9.1 to 1.3 W/(m K). These results were also consistent with the trend of thermal stage 2 of ultrafast experiments. In other words, the mixture of

https://dx.doi.org/10.1021/acs.jpclett.0c02886
J. Phys. Chem. Lett. 2020, 11, 9521−9527

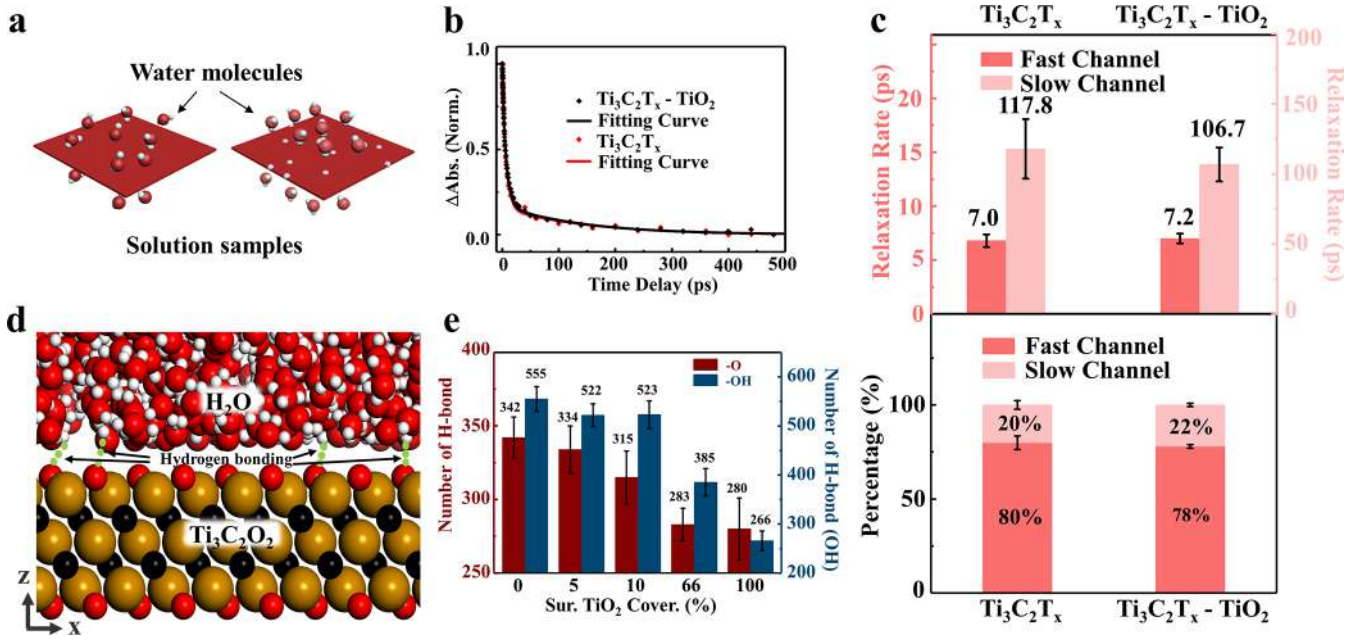

Figure 5. (a) Demonstration of two samples in water (the left one without oxidization and the right one with oxidization (white dots)). (b) Dynamic curves and fitting thermal dissipations. Dots are experimental data and lines are fitting curves. (c) Ultrafast relaxation time constants for the two samples under two thermal relaxation channels and the ratio of the two channels during the total relaxation. (d) Atomistic structure of $Ti_3C_2O_2$ water interface. (e) The numbers of H-bonds for $Ti_3C_2O_2$ and $Ti_3C_2(OH)_2$ systems with different oxidization ratio.

an oxidized particle on the flake surface could block the lateral thermal transport for the $Ti_3C_2T_x$ films. Generally, in two-dimensional materials, the lateral thermal transfer rate is generally faster than the interfacial thermal migration. But under real experimental conditions, the lateral thermal transfer including the part of in-plan in a nanosheets and the parallel transfer between two nanosheets. The parallel transfer between two nanosheets is a smaller contacted area than the perpendicular transfer. Therefore, the heat transfer is slower in the lateral direction. Additionally, once the $Ti_3C_2T_x$ flakes were dissolved into water, it would be well dispersed with surrounding water molecules. The interaction occurring at the $Ti_3C_2T_x$ flake surface switched from flake−flake to flake−water. Thus, for the hot flake shown in Figure 5a, interfacial thermal dissipation acceptors were changed from the cold flake to the attached water molecules. We then detected the thermal dissipation of the two samples with an ultrafast pump probe experiment. As shown in Figure 5b, the two dynamic decay curves overlapped quite well, which suggested the same energy migration mechanism at the $Ti_3C_2T_x$ surface. Figure 5c presented the thermal relaxation parameters of the two samples. The results showed that most thermal energy (~80%) would dissipate through the fast-interfacial channel within 7 ps. On the basis of our experimental results, the ~5% oxidation at the flake surface could not retard or accelerate the thermal decay. To understand the molecular level origins, we then performed MD simulation at $Ti_3C_2T_2$−water (T_2 = O_2, $(OH)_2$) interfaces. We evaluated the hydrogen bonds formed between $Ti_3C_2O_2$/$Ti_3C_2(OH)_2$ (with different oxidization ratio) and water molecules (Figure 5e) (time evolution data were shown in Figure S11). Noticeably, for the 100% oxidation case ($Ti_3C_2O_2$), the number of H-bonds declined 17.6% compared with the case without oxidization. This denoted the TiO_2 at the $Ti_3C_2T_x$ surface could also form hydrogen bonds with water. A similar observation could be found in $Ti_3C_2(OH)_2$ samples. For the slight oxidation cases (0−11%), the capabilities to form hydrogen bonds at the interface were quite similar. The previous results had demonstrated the interfacial chemical bonds would play the dominating role in the thermal migration process.[25,31] Thus, the results showed that the slight oxidation could not tune the thermal migration pathways.

In summary, combining ultrafast spectroscopy and MD simulation, we presented the thermal migration pathway of MXene flakes with surface oxidization in different conditions. We found the slight oxidation at a flake could significantly facilitate interfacial thermal migration but retard lateral heat transport in a solid sample. In contrast, the slight oxidation could not alter the fast energy migration from the MXene surface group to the binding water molecules. Our findings provided the fundamental understanding of the thermal migration pathway modulation approach and could be potentially helpful in further various MXene related thermal applications and management.

■ ASSOCIATED CONTENT

Supporting Information

The Supporting Information is available free of charge at https://pubs.acs.org/doi/10.1021/acs.jpclett.0c02886.

TEM images, absorption spectra, AFM micrograph, atomisitic structures, mechanism of RNEMD, temperature profiles, variation of thermal boundary conductance ratio and boundary distance ratio with respect to TiO_2 coverage, RDFs at different oxygen levels, number of new bonds formed per coverage and time, and table of numerical relation between boundary distance and TBC; Supporting notes discussing sample preparation and instrumentation, atomistic simulation, and the molecular dynamics (PDF)

https://dx.doi.org/10.1021/acs.jpclett.0c02886
J. Phys. Chem. Lett. 2020, 11, 9521−9527

AUTHOR INFORMATION

Corresponding Authors

Jiebo Li − *Institute of Medical Photonics, Beijing Advanced Innovation Center for Biomedical Engineering, School of Biological Science and Medical Engineering, Beihang University, Beijing 100191, P.R. China;* orcid.org/0000-0002-2295-6666; Email: jiebo39@buaa.edu.cn

Kaijun Yuan − *State Key Laboratory of Molecular Reaction Dynamics, Dalian Institute of the Chemical Physics, Chinese Academy of Sciences, Dalian, Liaoning 116023, P.R.China;* orcid.org/0000-0002-5108-8984; Email: kjyuan@dicp.ac.cn

Xin Yan − *School of Mechanical Engineering and Automation, Beihang University, Beijing 100191, P. R. China; Advanced Manufacturing Center, Ningbo Institute of Technology, Beihang University, Ningbo 315100, P. R. China;* orcid.org/0000-0002-6858-9152; Email: yan_xin@buaa.edu.cn

Authors

Qi Zhang − *State Key Laboratory of Molecular Reaction Dynamics, Dalian Institute of the Chemical Physics, Chinese Academy of Sciences, Dalian, Liaoning 116023, P.R.China; University of Chinese Academy of Sciences, Beijing 100049, China;* orcid.org/0000-0001-7500-5496

Yu Chen − *School of Mechanical Engineering and Automation, Beihang University, Beijing 100191, P. R. China*

Yifan Zhang − *Institute of Medical Photonics, Beijing Advanced Innovation Center for Biomedical Engineering, School of Biological Science and Medical Engineering, Beihang University, Beijing 100191, P.R. China*

Jingyong Sun − *National Laboratory for Aeronautics and Astronautics, Beihang University, Beijing 100191, P.R. China*

Mingjun Hu − *School of Materials Science and Engineering, Beihang University, Beijing 100191, China;* orcid.org/0000-0002-5474-6022

Xueming Yang − *State Key Laboratory of Molecular Reaction Dynamics, Dalian Institute of the Chemical Physics, Chinese Academy of Sciences, Dalian, Liaoning 116023, P.R.China;* orcid.org/0000-0001-6684-9187

Complete contact information is available at: https://pubs.acs.org/10.1021/acs.jpclett.0c02886

Author Contributions

¶Q.Z., Y.C. and Y.Z. contributed equally.

Notes

The authors declare no competing financial interest.

ACKNOWLEDGMENTS

This work is supported by the National Natural Science Foundation of China (NSFC-21803006), the Fundamental Research Funds for the Central Universities. M.H. acknowledges the National Natural Science Foundation of China (21771017 and 51702009). X. Yan acknowledge the National Natural Science Foundation of China (11902014). K.Y. acknowledges the National Natural Science Foundation of China (21873099 and 21673232). Y.C. and X. Yan acknowledge the insightful discussion with Dr. Shengjie Tang. X. Yan, J.L., and Y.C. acknowledge Information Office of Beihang University for the supply of High Performance Computing Platform.

REFERENCES

(1) Gogotsi, Y.; Anasori, B. The Rise of MXenes. *ACS Nano* **2019**, *13*, 8491−8494.

(2) Anasori, B.; Lukatskaya, M. R.; Gogotsi, Y. 2D Metal Carbides and Nitrides (MXenes) for Energy Storage. *Nat. Rev. Mater.* **2017**, *2*, 16098.

(3) Shahzad, F.; Alhabeb, M.; Hatter, C. B.; Anasori, B.; Man Hong, S.; Koo, C. M.; Gogotsi, Y. Electromagnetic Interference Shielding with 2D Transition Metal Carbides (MXenes). *Science* **2016**, *353*, 1137−1140.

(4) Ling, Z.; Ren, C. E.; Zhao, M. Q.; Yang, J.; Giammarco, J. M.; Qiu, J.; Barsoum, M. W.; Gogotsi, Y. Flexible and Conductive MXene Films and Nanocomposites with High Capacitance. *Proc. Natl. Acad. Sci. U. S. A.* **2014**, *111*, 16676−16681.

(5) Montazeri, K.; Currie, M.; Verger, L.; Dianat, P.; Barsoum, M. W.; Nabet, B. Mxene Photodetectors: Beyond Gold: Spin-Coated Ti_3C_2-Based MXene Photodetectors. *Adv. Mater.* **2019**, *31*, 1970307.

(6) Yasaei, P.; Tu, Q.; Xu, Y.; Verger, L.; Wu, J.; Barsoum, M.; Shekhawat, G.; Dravid, V. Mapping Hot-Spots at Heterogeneities of Few-Layer Ti_3C_2 MXene Sheets. *ACS Nano* **2019**, *13*, 3301−3309.

(7) Kim, H.; Alshareef, H. N. MXetronics: MXene-Enabled Electronic and Photonic Devices. *ACS Materials Letters* **2020**, *2*, 55−70.

(8) Dai, C.; Chen, Y.; Jing, X.; Xiang, L.; Yang, D.; Lin, H.; Liu, Z.; Han, X.; Wu, R. Two-Dimensional Tantalum Carbide (MXenes) Composite Nanosheets for Multiple Imaging-Guided Photothermal Tumor Ablation. *ACS Nano* **2017**, *11*, 12696−12712.

(9) Lin, H.; Wang, X.; Yu, L.; Chen, Y.; Shi, J. Two-Dimensional Ultrathin MXene Ceramic Nanosheets for Photothermal Conversion. *Nano Lett.* **2017**, *17*, 384−391.

(10) Wu, F.; Zheng, H.; Wang, W.; Wu, Q.; Zhang, Q.; Guo, J.; Pu, B.; Shi, X.; Li, J.; Chen, X.; Hong, W. Rapid Eradication of Antibiotic-Resistant Bacteria and Biofilms by MXene and Near-Infrared Light through Photothermal Ablation. *Sci. China Mater.* **2020**, DOI: 10.1007/s40843-020-1451-7.

(11) Cai, G.; Ciou, J.-H.; Liu, Y.; Jiang, Y.; Lee, P. S. Leaf-Inspired Multiresponsive MXene-Based Actuator for Programmable Smart Devices. *Sci. Adv.* **2019**, *5*, No. eaaw7956.

(12) Li, R.; Zhang, L.; Shi, L.; Wang, P. MXene Ti_3C_2: An Effective 2D Light-to-Heat Conversion Material. *ACS Nano* **2017**, *11*, 3752−3759.

(13) Hemmat, Z.; Yasaei, P.; Schultz, J. F.; Hong, L.; Majidi, L.; Behranginia, A.; Verger, L.; Jiang, N.; Barsoum, M. W.; Klie, R. F. Tuning Thermal Transport Through Atomically Thin $Ti_3C_2T_z$ MXene by Current Annealing in Vacuum. *Adv. Funct. Mater.* **2019**, *29*, 1805693.

(14) Habib, T.; Zhao, X.; Shah, S. A.; Chen, Y.; Sun, W.; An, H.; Lutkenhaus, J. L.; Radovic, M.; Green, M. J. Oxidation Stability of $Ti_3C_2T_x$ MXene Nanosheets in Solvents and Composite Films. *npj 2D Mater. Appl.* **2019**, *3*, 8.

(15) Zhang, C. J.; Pinilla, S.; McEvoy, N.; Cullen, C. P.; Anasori, B.; Long, E.; Park, S.-H.; Seral-Ascaso, A.; Shmeliov, A.; Krishnan, D.; Morant, C.; Liu, X.; Duesberg, G. S.; Gogotsi, Y.; Nicolosi, V. Oxidation Stability of Colloidal Two-Dimensional Titanium Carbides (MXenes). *Chem. Mater.* **2017**, *29*, 4848−4856.

(16) Chae, Y.; Kim, S. J.; Cho, S.-Y.; Choi, J.; Maleski, K.; Lee, B.-J.; Jung, H.-T.; Gogotsi, Y.; Lee, Y.; Ahn, C. W. An Investigation into the Factors Governing the Oxidation of Two-Dimensional Ti_3C_2 MXene. *Nanoscale* **2019**, *11*, 8387−8393.

(17) Lotfi, R.; Naguib, M.; Yilmaz, D. E.; Nanda, J.; van Duin, A. C. T. A Comparative Study on the Oxidation of Two-Dimensional Ti_3C_2 MXene Structures in Different Environments. *J. Mater. Chem. A* **2018**, *6*, 12733−12743.

(18) Xia, F.; Lao, J.; Yu, R.; Sang, X.; Luo, J.; Li, Y.; Wu, J. Ambient Oxidation of Ti_3C_2 MXene Initialized by Atomic Defects. *Nanoscale* **2019**, *11*, 23330−23337.

(19) Li, J.; Qin, R.; Yan, L.; Chi, Z.; Shan, G. Plasmonic Light Illumination Creates a Channel To Achieve Fast Degradation of $Ti_3C_2T_x$ Nanosheets. *Inorg. Chem.* **2019**, *58*, 7285−7294.

(20) Low, J.; Zhang, L.; Tong, T.; Shen, B.; Yu, J. TiO_2/MXene Ti_3C_2 Composite with Excellent Photocatalytic CO_2 Reduction Activity. *J. Catal.* **2018**, *361*, 255−266.
(21) Xiong, C.; Wang, Z.; Peng, X.; Guo, Y.; Xu, S.; Zhao, T. Bifunctional Effect of Laser-Induced Nucleation-Preferable Microchannels and In-Situ Formed LiF SEI in MXenes for Stable Lithium-Metal Batteries. *J. Mater. Chem. A* **2020**, *8*, 14114−14125.
(22) Chertopalov, S.; Mochalin, V. N. Environment-Sensitive Photoresponse of Spontaneously Partially Oxidized Ti_3C_2 MXene Thin Films. *ACS Nano* **2018**, *12*, 6109−6116.
(23) Zhang, Q.; Yan, L.; Yang, M.; Wu, G.; Hu, M.; Li, J.; Yuan, K.; Yang, X. Ultrafast Transient Spectra and Dynamics of MXene ($Ti_3C_2T_x$) in Response to Light Excitations of Various Wavelengths. *J. Phys. Chem. C* **2020**, *124*, 6441−6447.
(24) Li, J.; Zhang, Q.; Yan, L.; Wu, G.; Hu, M.; Lin, X.; Yuan, K.; Yang, X. Ultrafast Flash Energy Conductance at MXene-Surfactant Interface and Its Molecular Origins. *Adv. Mater. Interfaces* **2019**, *6*, 1901461.
(25) Li, J.; Chi, Z.; Qin, R.; Yan, L.; Lin, X.; Hu, M.; Shan, G.; Chen, H.; Weng, Y.-X. Hydrogen Bond Interaction Promotes Flash Energy Transport at MXene-Solvent Interface. *J. Phys. Chem. C* **2020**, *124*, 10306−10314.
(26) Yan, Z.; Chen, L.; Yoon, M.; Kumar, S. Phonon Transport at the Interfaces of Vertically Stacked Graphene and Hexagonal Boron Nitride Heterostructures. *Nanoscale* **2016**, *8*, 4037−4046.
(27) Li, J.; Chen, H.; Miranda, A.; Yuan, K.; Chen, Y.; Shen, Y.; Jiang, B.; Zhang, Y.; Guo, X.; Zheng, J. Non-Resonant Vibrational Energy Transfer on Metal Nanoparticle/Liquid Interface. *J. Phys. Chem. C* **2016**, *120*, 25173−25179.
(28) Momeni, K.; Ji, Y.; Wang, Y.; Paul, S.; Neshani, S.; Yilmaz, D. E.; Shin, Y. K.; Zhang, D.; Jiang, J.-W.; Park, H. S.; Sinnott, S.; van Duin, A.; Crespi, V.; Chen, L.-Q. Multiscale Computational Understanding and Growth of 2D Materials: a Review. *npj Comp. Mater.* **2020**, *6*, 22.
(29) Lin, C.; Xuguo, S.; Nanjie, Y.; Xing, Z.; Xiaoze, D.; Jun, L. Measurement and Analysis of Thermal Conductivity of $Ti_3C_2T_x$ MXene Films. *Materials* **2018**, *11*, 1701.
(30) El-Mahallawi, I. S.; Shash, A. Y.; Amer, A. E. Nanoreinforced Cast Al-Si Alloys with Al_2O_3, TiO_2 and ZrO_2 Nanoparticles. *Metals* **2015**, *5*, 802−821.
(31) Losego, M. D.; Grady, M. E.; Sottos, N. R.; Cahill, D. G.; Braun, P. V. Effects of Chemical Bonding on Heat Transport across Interfaces. *Nat. Mater.* **2012**, *11*, 502−506.

https://dx.doi.org/10.1021/acs.jpclett.0c02886
J. Phys. Chem. Lett. 2020, 11, 9521−9527